PHANGS–JWST First Results: Dust-embedded Star Clusters in NGC 7496 Selected via 3.3 μm PAH Emission

M. Jimena Rodríguez[1,2], Janice C. Lee[1,3], B. C. Whitmore[4], David A. Thilker[5], Daniel Maschmann[1,6],
Rupali Chandar[7], Sinan Deger[8], Médéric Boquien[9], Daniel A. Dale[10], Kirsten L. Larson[11], Thomas G. Williams[12,13],
Hwihyun Kim[3], Eva Schinnerer[13], Erik Rosolowsky[14], Adam K. Leroy[15,16], Eric Emsellem[17,18],
Karin M. Sandstrom[19], J. M. Diederik Kruijssen[20], Kathryn Grasha[21,22], Elizabeth J. Watkins[23], Ashley. T. Barnes[24],
Mattia C. Sormani[25], Jaeyeon Kim[25], Gagandeep S. Anand[4], Mélanie Chevance[20,25], F. Bigiel[24],
Ralf S. Klessen[25,26], Hamid Hassani[14], Daizhong Liu[27], Christopher M. Faesi[28], Yixian Cao[27], Francesco Belfiore[29],
Ismael Pessa[13,30], Kathryn Kreckel[23], Brent Groves[31], Jérôme Pety[32,33], Rémy Indebetouw[34,35], Oleg V. Egorov[23],
Guillermo A. Blanc[36,37], Toshiki Saito[38], and Annie Hughes[39]

[1] Steward Observatory, University of Arizona, 933 North Cherry Avenue, Tucson, AZ 85721, USA; jimenarodriguez@arizona.edu
[2] Instituto de Astrofísica de La Plata, CONICET–UNLP, Paseo del Bosque S/N, B1900FWA La Plata, Argentina
[3] Gemini Observatory/NSF's NOIRLab, 950 North Cherry Avenue, Tucson, AZ, USA
[4] Space Telescope Science Institute, 3700 San Martin Drive, Baltimore, MD 21218, USA
[5] Department of Physics and Astronomy, The Johns Hopkins University, Baltimore, MD 21218 USA
[6] Sorbonne Université, LERMA, Observatoire de Paris, PSL university, CNRS, F-75014, Paris, France
[7] Ritter Astrophysical Research Center, University of Toledo, Toledo, OH 43606, USA
[8] The Oskar Klein Centre for Cosmoparticle Physics, Department of Physics, Stockholm University, AlbaNova, Stockholm, SE-106 91, Sweden
[9] Centro de Astronomía (CITEVA), Universidad de Antofagasta, Avenida Angamos 601, Antofagasta, Chile
[10] Department of Physics and Astronomy, University of Wyoming, Laramie, WY 82071, USA
[11] AURA for the European Space Agency (ESA), Space Telescope Science Institute, 3700 San Martin Drive, Baltimore, MD 21218, USA
[12] Sub-department of Astrophysics, Department of Physics, University of Oxford, Keble Road, Oxford OX1 3RH, UK
[13] Max-Planck-Institut für Astronomie, Königstuhl 17, D-69117 Heidelberg, Germany
[14] Department of Physics, University of Alberta, Edmonton, AB, T6G 2E1, Canada
[15] Department of Astronomy, The Ohio State University, 140 West 18th Avenue, Columbus, Ohio 43210, USA
[16] Center for Cosmology and Astroparticle Physics, 191 West Woodruff Avenue, Columbus, OH 43210, USA
[17] European Southern Observatory, Karl-Schwarzschild-Straße 2, D-85748 Garching, Germany
[18] Univ Lyon, Univ Lyon1, ENS de Lyon, CNRS, Centre de Recherche Astrophysique de Lyon UMR5574, F-69230 Saint-Genis-Laval, France
[19] Center for Astrophysics & Space Sciences, University of California, San Diego, 9500 Gilman Drive, San Diego, CA 92093, USA
[20] Cosmic Origins Of Life (COOL) Research DAO,[40]
[21] Research School of Astronomy and Astrophysics, Australian National University, Canberra, ACT 2611, Australia
[22] ARC Centre of Excellence for All Sky Astrophysics in 3 Dimensions (ASTRO 3D), Australia
[23] Astronomisches Rechen-Institut, Zentrum für Astronomie der Universität Heidelberg, Mönchhofstraße 12-14, D-69120 Heidelberg, Germany
[24] Argelander-Institut für Astronomie, Universität Bonn, Auf dem Hügel 71, D-53121, Bonn, Germany
[25] Universität Heidelberg, Zentrum für Astronomie, Institut für Theoretische Astrophysik, Albert-Ueberle-Straße 2, D-69120 Heidelberg, Germany
[26] Universität Heidelberg, Interdisziplinäres Zentrum für Wissenschaftliches Rechnen, Im Neuenheimer Feld 205, D-69120 Heidelberg, Germany
[27] Max-Planck-Institut für Extraterrestrische Physik (MPE), Giessenbachstr. 1, D-85748 Garching, Germany
[28] University of Connecticut, Department of Physics, 196A Auditorium Road, Unit 3046, Storrs, CT 06269, USA
[29] INAF–Arcetri Astrophysical Observatory, Largo E. Fermi 5, I-50125, Florence, Italy
[30] Leibniz-Institut für Astrophysik Potsdam (AIP), An der Sternwarte 16, D-14482 Potsdam, Germany
[31] International Centre for Radio Astronomy Research, University of Western Australia, 7 Fairway, Crawley, 6009 WA, Australia
[32] IRAM, 300 rue de la Piscine, F-38400 Saint Martin d'Hères, France
[33] LERMA, Observatoire de Paris, PSL Research University, CNRS, Sorbonne Universités, F-75014 Paris, France
[34] National Radio Astronomy Observatory, 520 Edgemont Road, Charlottesville, VA 22903, USA
[35] University of Virginia, 530 McCormick Road, Charlottesville, VA 22904, USA
[36] The Observatories of the Carnegie Institution for Science, 813 Santa Barbara Street, Pasadena, CA, USA
[37] Departamento de Astronomía, Universidad de Chile, Camino del Observatorio 1515, Las Condes, Santiago, Chile
[38] National Astronomical Observatory of Japan, 2-21-1 Osawa, Mitaka, Tokyo, 181-8588, Japan
[39] IRAP, Université de Toulouse, CNRS, CNES, UPS, (Toulouse), France

Abstract

The earliest stages of star formation occur enshrouded in dust and are not observable in the optical. Here we leverage the extraordinary new high-resolution infrared imaging from JWST to begin the study of dust-embedded star clusters in nearby galaxies throughout the Local Volume. We present a technique for identifying dust-embedded clusters in NGC 7496 (18.7 Mpc), the first galaxy to be observed by the PHANGS–JWST Cycle 1 Treasury Survey. We select sources that have strong 3.3 μm PAH emission based on a F300M − F335M color excess and identify 67 candidate embedded clusters. Only eight of these are found in the PHANGS-HST optically

---

[40] coolresearch.io

selected cluster catalog, and all are young (six have SED fit ages of ∼1 Myr). We find that this sample of embedded cluster candidates may significantly increase the census of young clusters in NGC 7496 from the PHANGS-HST catalog; the number of clusters younger than ∼2 Myr could be increased by a factor of 2. Candidates are preferentially located in dust lanes and are coincident with the peaks in the PHANGS-ALMA CO (2–1) maps. We take a first look at concentration indices, luminosity functions, SEDs spanning from 2700 Å to 21 μm, and stellar masses (estimated to be between ∼10^4 and 10^5 $M_\odot$). The methods tested here provide a basis for future work to derive accurate constraints on the physical properties of embedded clusters, characterize the completeness of cluster samples, and expand analysis to all 19 galaxies in the PHANGS–JWST sample, which will enable basic unsolved problems in star formation and cluster evolution to be addressed.

Unified Astronomy Thesaurus concepts: Star formation (1569); Star clusters (1567); Young star clusters (1833); Spiral galaxies (1560); Surveys (1671); Interstellar dust (836); Polycyclic aromatic hydrocarbons (1280)

1. Introduction

Star clusters are formed in the densest parts of giant molecular clouds (Lada & Lada 2003; Elmegreen 2008; Kruijssen 2012). During their formation and early evolution, they remain surrounded by dust and molecular gas, causing them to be heavily obscured at optical wavelengths and often only detectable at infrared and longer wavelengths. Until now, such young objects were mostly identified using observations of the radio continuum (Johnson et al. 2003) or dust continuum in combination with molecular gas lines (Leroy et al. 2018). Infrared studies of the star clusters inside such nurseries have so far mainly occurred in the Milky Way, Magellanic Clouds, and Local Group (e.g., Großschedl et al. 2019).

Since most stars form in clustered environments (Lada & Lada 2003), embedded clusters represent a very early, critical stage in the star formation process. Therefore, the study of these systems is essential for understanding the mechanisms that drive star formation overall and the properties and evolution of star cluster populations in galaxies.

Previous studies suggest that star clusters remain in this embedded phase within their natal cloud for only a few megayears (∼2–5 Myr; e.g., Whitmore et al. 2014b; Corbelli et al. 2017; Grasha et al. 2018, 2019; Messa et al. 2021; Kim et al. 2021, 2023; Whitmore et al. 2023, this volume). However, it has not been possible to obtain complete samples of embedded clusters beyond the Local Group to constrain these durations more directly, as the angular resolution of previous infrared facilities could not resolve the parsec scales required to identify clusters at larger distances.

The powerful new infrared capabilities of JWST enable embedded young star clusters throughout nearby galaxies to be identified and studied statistically. Complete samples of embedded clusters from PHANGS–JWST, combined with the PHANGS Hubble Space Telescope (HST), Atacama Large Millimeter/submillimeter Array (ALMA), and MUSE data sets, will allow basic open issues in star and cluster formation to be addressed, such as the fraction of star formation that occurs in clusters (cluster formation efficiency), timescales for the clearing of the natal dust and gas, the conditions that lead to cluster formation, and the dependence of these parameters on galactic environment.

In this pilot study, we identify candidate embedded clusters in NGC 7496 using PHANGS–JWST NIRCam and PHANGS-HST UV-optical imaging. We find that selection based on an excess in the F300M − F335M color, indicating polycyclic aromatic hydrocarbon (PAH) 3.3 μm emission, effectively identifies the youngest dusty star clusters. We take a first look at their properties and compare with the census of optically selected clusters in the PHANGS-HST catalog. The rest of this

paper is organized as follows. In Section 2, we summarize the observations of NGC 7496 taken as part of the PHANGS–JWST Treasury program. In Section 3, we identify a small set of prototype embedded clusters with strong PAH 3.3 μm emission and use their measured properties to define selection criteria to identify a larger sample of candidate young, embedded clusters. In Section 4, we estimate the masses of the newly identified clusters and take a first look at their luminosity functions (LFs) at 2 and 3 μm. We compare this new embedded cluster sample with the optically selected PHANGS-HST catalog in Section 5 and also examine other properties of the sources, including concentration indices (CIs) and UV-IR spectral energy distributions (SEDs), which also incorporate photometry from PHANGS–JWST MIRI imaging. We summarize our main conclusions and outline future work in Section 6.

2. Data

The PHANGS–JWST Cycle 1 Treasury program observed its first target, the dusty barred spiral galaxy NGC 7496 located at 18.7 Mpc (Shaya et al. 2017; Kourkchi et al. 2020; Anand et al. 2021), on 2022 July 6. The data were released (simultaneously to the team and public) on 2022 July 14. All 19 galaxies in the PHANGS–JWST sample will eventually be imaged with NIRCam and MIRI from 2.0 to 21 μm using eight filters (NIRCam: F200W, F300M, F335M, and F360M; MIRI: F770W, F1000W, F1130W, and F2100W). Full details of the observing strategy and data reduction are given in the PHANGS–JWST survey description paper in this volume (Lee et al. 2023).

In this analysis, we examine the JWST data together with UV-optical imaging in five filters from the PHANGS-HST survey (Lee et al. 2023; F275W, F336W, F438W, F555W, and F814W). We compare our dust-embedded clusters with the sample from the PHANGS-HST cluster catalog (Thilker et al. 2022; Turner et al. 2021; Deger et al. 2022; Lee et al. 2023), which provides age and stellar mass estimates from SED fitting in NGC 7496. Here we consider the 263 clusters in the HST catalog that have passed human visual inspection and are classified as class 1 (symmetric compact cluster) and class 2 (asymmetric compact cluster; Whitmore et al. 2021; Deger et al. 2022). This PHANGS-HST sample spans a wide range of properties, with ages between 1 Myr and 13.7 Gyr and masses between 500 and 4.6×10^6 $M_\odot$ with a median of 1.5×10^4 $M_\odot$. Of these, 131 are 10 Myr and younger, with masses between 600 and 4.3×10^5 $M_\odot$ with a median of 8000 $M_\odot$.

3. Methodology

3.1. Identification of Embedded Cluster Prototypes

To begin our studies of dust-embedded young star clusters with JWST, we visually inspect the images to identify a small sample of sources that are obvious candidates for dusty clusters and can serve as prototypes to guide our analysis. We look for bright compact sources in the NIRCam F335M filter that also appear in at least one other PHANGS–JWST NIRCam image (F200W, F300M, or F360M) but are either faint or not visible by eye in the PHANGS-HST UV-optical images ($A_V \gtrsim 10$). We choose compact objects that are slightly more extended than point sources (i.e., FWHM $\gtrsim 1.8$ pixels ~ 10 pc), following a process similar to that for optical star clusters in PHANGS-HST imaging (Thilker et al. 2022; Whitmore et al. 2021; Deger et al. 2022; Lee et al. 2023). We choose to start our inspection with the NIRCam F335M image because it is the highest-resolution image obtained by PHANGS–JWST that captures PAH emission and hot dust.[41] We identify an initial set of 12 prototypical clusters. The bottom panels of Figure 1 show examples of these prototypes marked in yellow. Aperture photometry is performed to examine the properties of these objects and to develop selection criteria to select embedded cluster candidates, as discussed further in the next section.

3.2. Source Detection and Photometry

To obtain positions and photometry for our set of 12 prototype embedded clusters, as well as search for embedded clusters in a more systematic way, we use routines in the PHOTUTILS (Bradley et al. 2022) Astropy package for photometry. First, we use the peak-finding algorithm *find_peaks* to detect sources in the F335M image. The level of the background varies significantly across the image. So, in order to estimate local background levels, we use the function SExtractorBackground to build a 2D model of the background. Then, we search for local maxima in square regions that are 11 pixels on a side.

To derive accurate source positions, we use the function *centroid_quadratic*, which determines the centroid by fitting 2D quadratic polynomials. We extract photometry from a circular aperture with a radius of $0\rlap.{''}093$ (3 NIRCam short-wavelength pixels) that encloses more than 50% of the energy for a point source ($0\rlap.{''}073$) in the F335W filter. We subtract the background computed from an annulus between $0\rlap.{''}217$ and $0\rlap.{''}31$ away from the source center. The units of the NIRCam imaging are megajanskys per steradian, so we multiply by the pixel area in steradians, given by the parameter *PIXAR_SR* in the header of the image, to obtain flux densities in megajanskys. We then convert the measured flux densities into the AB magnitudes using the usual expression:

$$m_{\mathrm{AB}} = -2.5 \log_{10}\left(\frac{f_\nu}{3\,631 \times 10^{-6}\ \mathrm{MJy}}\right).$$

For this initial analysis, we forgo aperture corrections to the photometry to calculate total source fluxes. The measurement of accurate total fluxes for individual clusters across the PHANGS–JWST filter set will be the subject of dedicated future work to address the challenges presented by the 10-fold decrease in resolution from 2 to 21 μm. Nevertheless, our

sample selection strategy, which is primarily based on the F300M – F335M color (described in Section 3), should not be greatly affected, since the resolution in these adjacent bands is quite similar, with a difference in the point-spread function (PSF) FWHM of only $0\rlap.{''}011$.

3.3. Selection Criteria for Embedded Cluster Candidates

In Figure 2, we show color–magnitude diagrams (CMDs) based on F335M and F300M photometry; the former captures flux from the PAH 3.3 μm feature, while the latter primarily probes the stellar and dust continuum (Lee et al. 2023; Sandstrom et al. 2023a, 2023b; Chastenet et al. 2023a, 2023b, this volume). Panel (a) in Figure 2 shows the 12 visually identified prototype embedded clusters (yellow stars) together with the sample of F335M sources detected using Photutils *find_peaks* (black dots). This latter sample is comprised of a mixture of sources including stellar clusters of different ages; main sequence, red giant branch, and asymptotic giant branch stars; and background galaxies.

These CMDs are analogous to those commonly used to select emission-line sources in extragalactic narrowband imaging surveys (e.g., Ly et al. 2011; Lee et al. 2012), and similar strategies can be adopted to identify and characterize sources with PAH emission. Sources that show a significant F300M − F335M color excess (i.e., a continuum-subtracted F335M flux) are identified as PAH emitters. The locus of points around F300M − F335M = 0 represents continuum sources with little to no PAH emission. These objects are typically associated with star clusters older than 10 Myr. as shown in panel (c) of Figure 2. Not surprisingly, this distribution becomes broader at fainter F335M magnitudes due to increasing noise in the F300M − F335M measurement (compare with Figure 3 in Lee et al. 2012). Sources with PAH emission show significant F300M − F335M color excess and are found to the right of the locus, and we find that all 12 prototypes are in this region.

Based on this clear separation in the CMD, we select a larger sample of bright PAH emitters for examination, i.e., F300M − F335M > 0.3, F335M < 24, and F300M < 25. This selection provides a sample of 67 objects, shown with cyan symbols in panel (a) of Figure 2. In this figure, the lines indicate the limits F300M − F335M > 0.3 and F335M < 24. We note there are additional sources (beyond the 67 cyan candidates) that fall inside this box; however, these sources are fainter than F300M = 25 mag and not included in our sample.

We visually inspect each of these 67 cluster candidates and divide them into three categories as follows.

1. Embedded: optical emission very faint or undetected, similar to the 12 prototype objects ($N = 28$).
2. Intermediate/ambiguous: optical emission detected, but it is not clear whether the optical source is the counterpart to the F335M source due to positional differences, and lower resolution at 3 μm ($N = 16$).
3. Visible/exposed: clear optical counterpart ($N = 23$).

Examples of objects in each category are shown in Figure 1. We will compare our new, dust-embedded cluster sample with the optically selected PHANGS-HST catalog in Section 5.

4. Results

Luminosity and mass functions for the youngest cluster populations in galaxies give direct constraints on the initial

---

[41] We do not use continuum-subtracted F335M images for visual inspection to avoid issues with residuals on the small spatial scales of interest here.
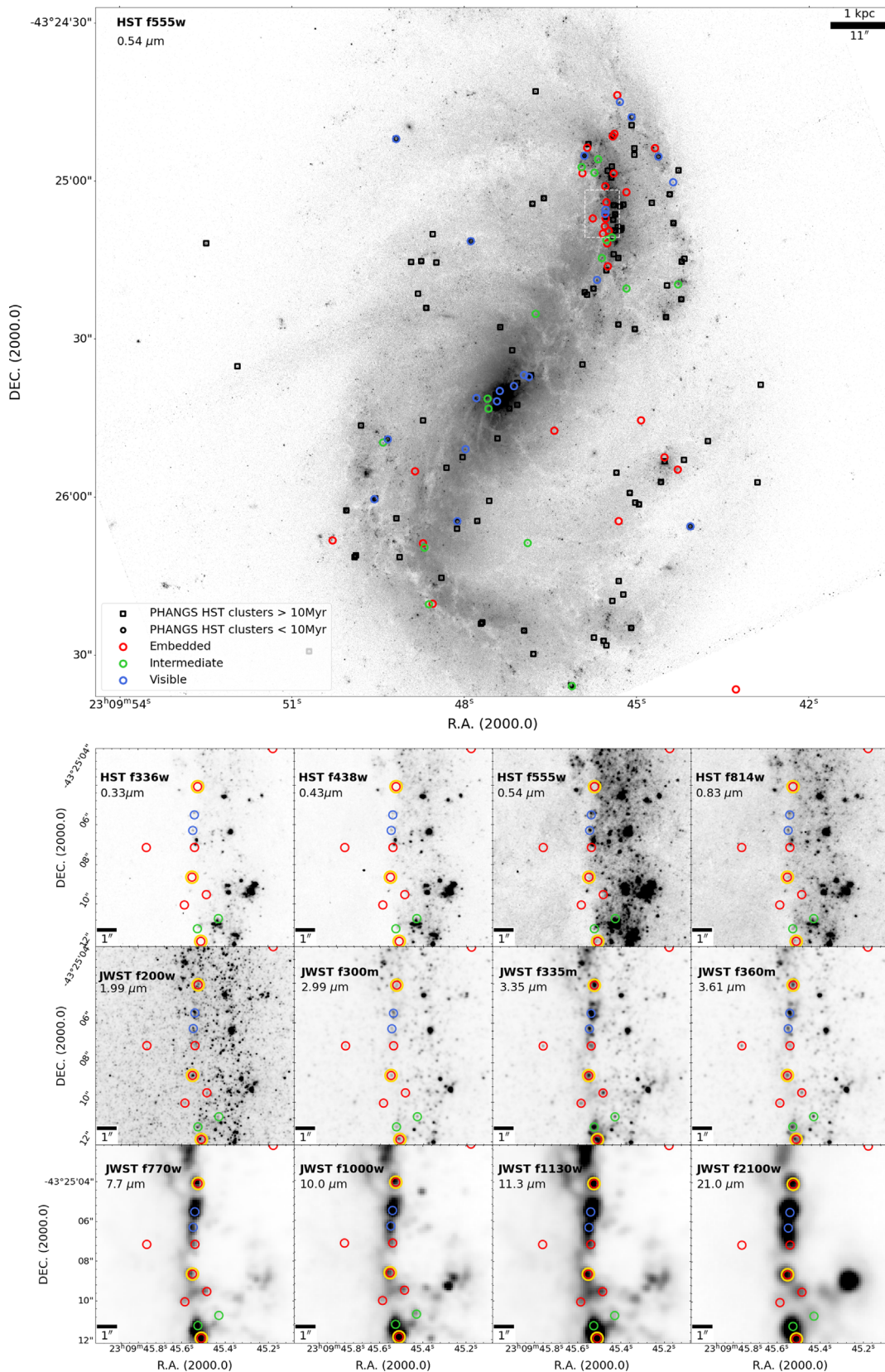
Figure 1. The top panel shows the PHANGS-HST WFC3 F555M image of NGC 7496. The sample of 67 PHANGS–JWST 3.3 μm–selected star cluster candidates is plotted with different colors according to their categories: embedded (red), partially embedded (green), and visible (blue). The locations of optically selected clusters from the PHANGS-HST catalog are also shown and distinguished by SED fit age (black squares for >10 Myr and black circles for <10 Myr). Only clusters brighter than F300M < 25 are included. The bottom panels show images in the HST-WFC3, JWST-NIRCam, and JWST-MIRI filters for the 10″ × 10″ region indicated by the white box in the top panel. The central wavelength of each filter is indicated in the panel label. The colored circles are the same as in the top panel. Clusters marked by an additional yellow circle are part of our prototype sample (see text for details). The comparison of this region in the optical HST images and IR from JWST clearly shows that the candidates fall along a dust lane, largely obscured in the HST bands.
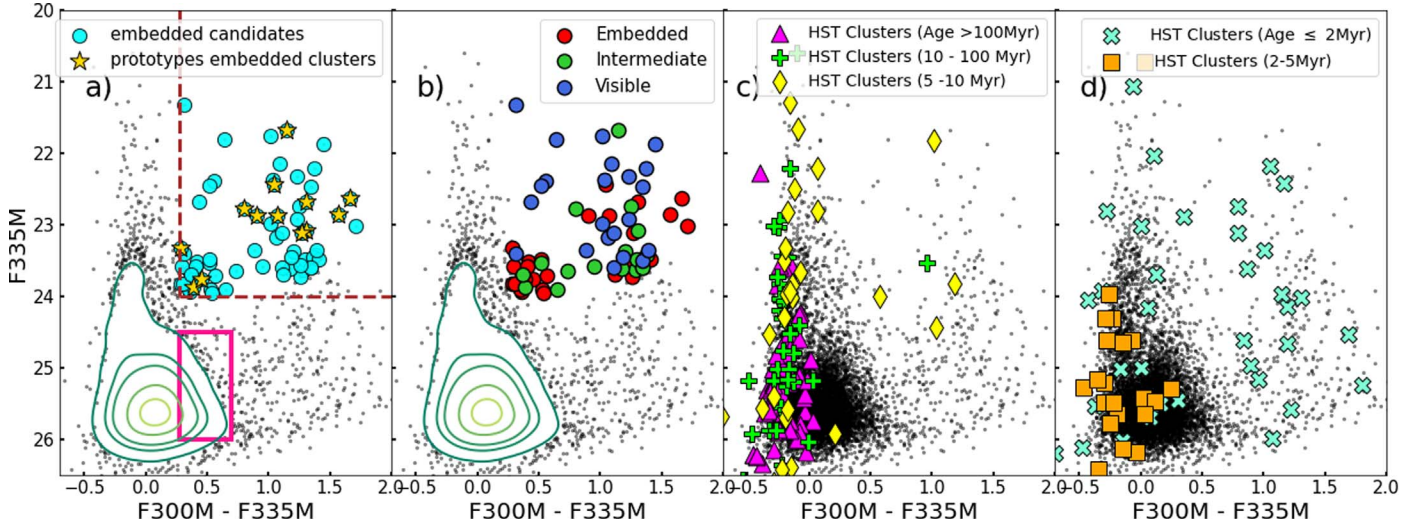
Figure 2. CMD F335M vs. F300M − F335M for NGC 7496. Magnitudes are in the AB system. In all panels, the black dots are F335M sources detected with Photutils *find_peaks*. Density contours for the densest parts of this diagram are shown in panels (a) and (b). In panel (a), yellow stars show the 12 prototype embedded clusters selected in our initial visual inspection. Based on the location in the CMD of these candidates, we select 67 embedded candidates (cyan circles). The dashed lines show the selection criteria: F300M − F335M > 0.3 and F335M < 24. The magenta box indicates a region where scatter due to the uncertainties in the color is large and is chosen for the purposes of illustrating the spatial distribution in Figure 5. Panel (b) shows the same extended sample of 67 candidates but differentiated by category: embedded (red), intermediate or partially embedded (green), and visible or exposed (blue). Panels (c) and (d) show for comparison the location in the CMD sources from the PHANGS-HST optical cluster catalog. Panel (c) shows clusters older than 100 Myr (magenta). As expected, these clusters fall around F300M − F335M = 0, indicating that these old sources do not have PAH emission. This panel also shows clusters with SED fit age estimates between 10 and 100 Myr (green plus signs) and 5–10 Myr (yellow diamonds), which also appear around F300M − F335M = 0. In contrast, about half of the clusters younger than 2 Myr shown in panel (d) (cyan crosses) are PAH emitters. Panel (d) also shows clusters between 2 and 5 Myr (orange squares), which mostly have little measured PAH emission.
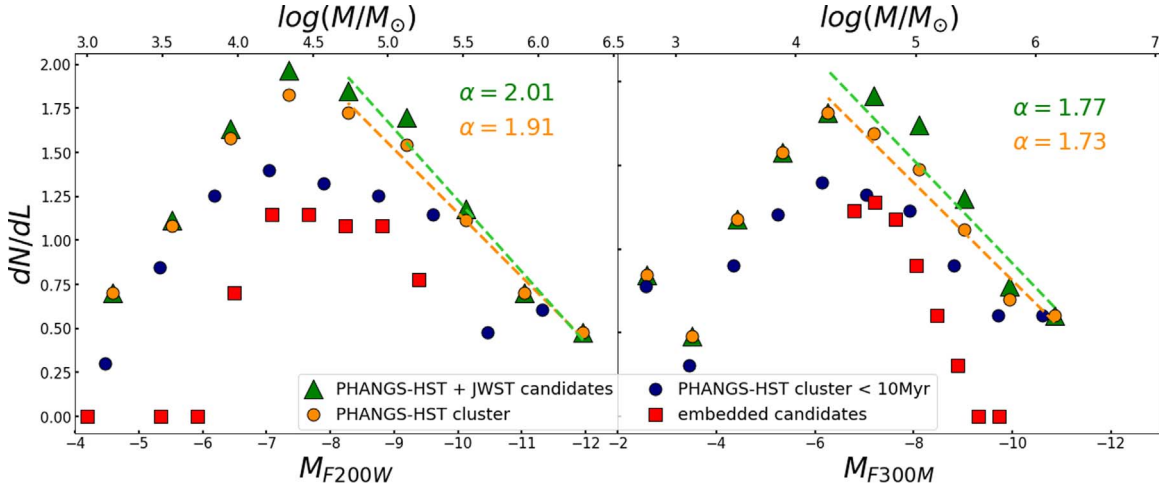
Figure 3. The LFs measured for different cluster samples are shown in the F200W (left) and F300M (right) filters. The red squares show distributions for the 67 dust-embedded cluster candidates from this work. The orange points show the LFs for PHANGS-HST–selected clusters at all ages ($N = 263$), and the blue dots are PHANGS-HST clusters younger than 10 Myr ($N = 131$). Green triangles indicate the LF of PHANGS-HST clusters plus the 67 embedded cluster candidates ($N = 330$). The green line shows the best-fit index to this last sample, while the orange line shows the fit for only the PHANGS-HST cluster distribution (orange circles). Our dust-embedded cluster sample (red squares) is not sufficiently deep to have many data points in the LF before the distribution begins to flatten, likely due to incompleteness, but by comparing the derived slopes with and without the embedded candidates, we observe that they are quite similar. The bright portion of each distribution appears to follow a trend that is consistent with that observed for the optically selected HST clusters. The upper axis indicates mass estimates from the method described in Section 4.2.

cluster mass function, analogous to the initial stellar mass function. One of the major weaknesses in current studies of star formation is that the fraction of the most recently formed dust-obscured clusters has been unknown and unaccounted for. These initial results provide a preview of the work with JWST that will measure these fundamental distributions.

4.1. Luminosity Function

For clusters with similar ages and reddening, the LF of clusters can serve as a proxy for their mass function. The LF

can be approximated, at least to first order, by a power-law shape of the form $dN/dL \propto L^\alpha$ (Whitmore et al. 1999; Fall 2006; Whitmore et al. 2014a). Values of the power-law index $\alpha \sim -2$ are typical for young star clusters (e.g., Larsen 2009; Whitmore et al. 2014a).

In Figure 3, we present the LFs of our embedded cluster candidates in the F200W and F300M bands, which sample flux from the stellar continuum, with some contribution from the dust continuum (red squares). These distributions increase starting from the brightest magnitudes (to the right), eventually flatten, and then drop off again (F200W filter). The flattening

toward fainter magnitudes is almost certainly due to incompleteness.

For comparison, we also show the LF of optically selected clusters from the PHANGS-HST survey (Thilker et al. 2022; Turner et al. 2021; Deger et al. 2022; Lee et al. 2023), with no restriction on age (shown in orange) and clusters with best-fit ages younger than 10 Myr (shown in blue). We also plot the LF of the combined cluster sample, i.e., PHANGS-HST clusters plus the 67 embedded candidates (shown with green triangles). The LF for the full HST+JWST cluster sample (green) has a best-fit power-law index of −2.01 in F200W and −1.77 for F300M (shown as the green lines in each panel). The fit over only the PHANGS-HST clusters (orange) gives very similar index values, −1.91 in F200W and −1.73 for F300M (orange lines). On the other hand, while there are only a few data points before our embedded cluster distribution (red points) flattens at magnitudes fainter than $M_{F200W} \geqslant -8$, the bright points suggest a behavior similar to the optically selected clusters. The LF in the F300M filter, however, appears to be steeper than the PHANGS-HST clusters. This difference could be due to the imposed selection criteria that involve cuts using the F300M filter (Section 3.3).

Based on our preliminary results, we suspect that the LF for embedded star clusters presents a similar shape to that for optical clusters. However, our sample is not large enough to derive accurate power-law indices. In future work, we will extend this work to the full sample of 19 PHANGS–JWST galaxies, which will be based on total fluxes computed with appropriate aperture corrections. A larger sample will better constrain the shape of the LF, as well as the embedded cluster mass function, which again, is effectively the initial cluster mass function. Comparison with what we have already learned for visible clusters will provide important insights into the survival of clusters in transition to becoming exposed/visible.

4.2. Estimate of Cluster Masses

To obtain initial stellar mass estimates for our 67 embedded cluster candidates, we fit a linear relation to obtain the mass-to-light ratio (e.g., Fall 2006; Larsen 2009) using clusters younger than 2 Myr in the PHANGS-HST catalog. In doing so, we obtain coefficients γ and C, where $\log(M/M_\odot) = \gamma \ \mathrm{mag} + C$. We use apparent magnitudes in the F200W and F300M bands, obtaining values of $\gamma = -2.35$, $C = 34.22$ and $\gamma = -2.43$, $C = 35.46$, respectively.

Using the relation for F200W, we obtain a range of masses between 6.4×10^2 and $1.1 \times 10^5 \ M_\odot$, with approximately 80% in the range 10^4–$10^5 \ M_\odot$. In the case of masses obtained from F300M, the values for our candidates start at $\sim 2 \times 10^4 \ M_\odot$ due to our imposed condition in the selection criteria (F300M < 25; see Section 3.3). We find that $\sim$88% of the sample is between this minimum value and $10^5 \ M_\odot$, with a few candidates reaching up to $\sim 5 \times 10^5 \ M_\odot$. The masses estimated from F200W and F300M are generally consistent to within a factor of a few, but clearly, from the vastly different values on the low end of the range, there are candidates ($n \sim 10$) with estimates that differ by up to a factor of $\sim$30. All of these candidates are embedded sources, which likely suffer from high extinction even at $2 \ \mu m$. In future work, we will provide more reliable mass estimates from SED fitting, as discussed further in the next section.

5. Discussion

We compare our sample of 67 dust-embedded cluster candidates with the PHANGS-HST human-inspected class $1 + 2$ cluster catalog ($N = 263$) and find that our analysis of the PHANGS–JWST imaging has identified 59 new embedded cluster candidates in NGC 7496. These objects are of particular importance because they are likely to be among the youngest clusters in this galaxy and are needed to construct a complete census. In this context, it is notable that the size of our new sample is comparable to the number of young HST clusters (59 younger than 2 Myr; 94 younger than 5 Myr) and may double the census of the population younger than $\sim$2 Myr.

Of the eight clusters in common between the two samples, we classify seven as visible/exposed and one as partially embedded/intermediate. All are found to be younger than 11 Myr (six having ages less than 1 Myr), with masses of ~ 1–$7 \times 10^4 \ M_\odot$. (As mentioned earlier, the full PHANGS-HST cluster sample, meanwhile, contains clusters as old as 13 Gyr.)

We can gain additional insight by examining the infrared properties of clusters of all ages from the optically selected PHANGS-HST sample. Panels (c) and (d) in Figure 2 show the location of clusters in different age intervals in the F300M − F335M color versus F335M magnitude diagram. In panel (c), we can see that clusters older than 100 Myr (magenta triangles) have F300M − F335M = 0, indicating that these older sources do not have PAH emission. This panel also shows that nearly all clusters with ages between 10 and 100 Myr (green plus signs) and 5–10 Myr (yellow diamonds) have F300M − F335M = 0. On the other hand, panel (d) shows that all HST clusters with an F300M − F335M color excess (i.e., strong PAH emission) have ages $\leqslant 2$ Myr (cyan crosses). These very young, optically selected clusters have a similar range of F300M − F335M values as our 67 embedded candidates, although most of them have a significantly fainter F335M magnitude. Panel (d) of Figure 2 also shows clusters with estimated ages between 2 and 5 Myr (orange squares). While a small fraction of these 2–5 Myr clusters have slightly higher F300M − F335M values than clusters older than 5 Myr, a surprising number of them show little to no PAH emission. Assuming that the age dating from PHANGS-HST is correct for these clusters, this result indicates that measurable PAH emission may drop very rapidly (in 2 Myr) in clusters of moderate mass.

We also examine the CIs of infrared and optically selected clusters. The CI provides a measure of the compactness of the source and is useful to distinguish between clusters and stars (e.g., Chandar et al. 2010; Whitmore et al. 2014b; Deger et al. 2022). In particular, Whitmore et al. (2023, this volume) found that a CI estimated from the JWST F200W filter significantly improves the separation of stars and clusters. The CI values were estimated following the procedure in Whitmore et al. (2023, this volume), as the magnitude difference measured between 1 and 4 pixel apertures (0″031 and 0″124) in the F200W filter. In Figure 4, we present the results. The vertical dashed line indicates CI =1.4, a limit to separate clusters from stars (Whitmore et al. 2023, this volume). The 67 dust-embedded clusters from this work are nearly all to the right of the line, meaning they are extended relative to a point source, although there are a few fainter objects that fall to the left of the line. The dispersion in the size measurements clearly increases toward fainter magnitudes.
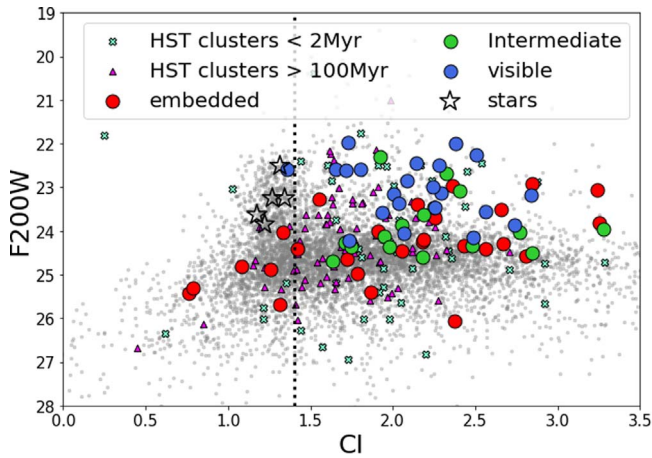
Figure 4. F200W magnitude vs. CI (measured as the difference in magnitude between circular apertures with 1 and 4 pixel radii). The vertical dashed line indicates CI =1.4, which can be used to distinguish clusters from stars (Whitmore et al. 2023, this volume). The colored circles represent our 67 cluster candidates as indicated; stars/point sources are represented by a star symbol. PHANGS-HST clusters younger than 2 Myr are small cyan small crosses, and those older than 100 Myr are small magenta triangles. The gray dots are all the sources detected in the F335M image.

Next, we examine the overall spatial distribution of the sample, as well as the location of our dust-embedded cluster candidates relative to other structures and components of the interstellar medium (ISM). In Figure 1, we see a strong concentration of embedded clusters (shown in red) along a dust lane in the northern spiral arm, which forms a ridge just next to young (age < 10 Myr) optically selected clusters. Jumping to the left panel of Figure 5, we see that the strongest PAH emitters (shown as green dots without an accompanying magenta circle) are mostly located where we see the most prominent dust features in the optical HST images, along the spiral arms. Sources with F300M − F335M > 0.3 but faint F335M magnitudes (see magenta box in Figure 2(a)) are enclosed with a magenta circle. Recall that we decided to apply cuts in magnitude to study only the brightest sources (F335M < 24 and F300M < 25) to simplify this initial analysis. However, by imposing these limits, weaker PAH emitters are excluded from inspection of the image; these appear to coincide with the more subtle dust lanes and potentially may also be dust-embedded clusters. In future work, we will test selection criteria that employ a color excess curve to identify fainter embedded clusters.

The middle and right panels of Figure 5 show a CO(2–1) ALMA image taken as part of the PHANGS-ALMA survey (Leroy et al. 2021) and the Hα VLT-MUSE image of NGC 7496 from the PHANGS-MUSE survey (Emsellem et al. 2022). Our 67 PAH-emitting sources are closely associated with molecular gas and current star formation. Only 9% of our candidates appear unassociated with significant peaks of CO emission, Hα, or both. These 9% all have no obvious optical counterpart in the HST images, and half have CI values similar to stars, indicating that they are very compact and possibly not embedded clusters.

Finally, we examine the SEDs of the embedded clusters from optical wavelengths with HST to the IR with NIRCam and MIRI, which provide further insights into their properties. We show preliminary SEDs of the 12 embedded cluster prototypes in Figure 6. These show a clear deficit in optical flux relative to

the infrared. In fact, we were able to identify possibly associated faint optical emission for only three of these objects. For the nine embedded clusters, without UV-optical detections, we show upper limits in the HST bands. For this first look, the photometric measurements in all bands have been performed with the same $0\farcs155$ aperture, which leads to a relative underestimate of the measured fluxes in the MIRI bands, as no aperture corrections have been applied as discussed before. To produce proper SEDs for these clusters in future work, we will need to correctly distinguish between crowded point sources and their corresponding diffuse PAH emission with more careful source extraction that takes the different PSFs into account. These are some of the challenges that need to be addressed in order to perform proper SED fitting for embedded clusters and more accurately constrain their physical properties (e.g., stellar masses, dust masses, ages, and reddenings). In addition to the distinctive PAH feature at 3.3 μm, we see a dip at 10 μm indicating silicate absorption, which is caused by protostellar envelopes (Crapsi et al. 2008) and has been observed in young stellar objects (e.g., Großschedl et al. 2019). This spectral feature supports our conclusion that these candidates are very young embedded clusters.

6. Summary and Conclusions

In this work, we have used new NIRCam imaging of the nearby spiral galaxy NGC 7496, the first galaxy to be observed for the PHANGS–JWST Treasury survey, to identify very young clusters embedded in natal dust and gas. Our selection method relies on detection of PAH 3.3 μm emission, which is closely associated with the ISM of very recently formed clusters.

We begin by identifying 12 prototype dust-obscured clusters based on visual inspection of both PHANGS–JWST NIRCam and PHANGS-HST optical images. We find that all 12 show strong PAH emission at 3.3 μm and fall in a region of the F335M versus F330M − F335M CMD that clearly separates from the vast majority of detections. To first order, the PAH emission at 3.3 μm appears to correlate with other dust emission (Sandstrom et al. 2023a, 2023b; Dale et al. 2023; Chastenet et al. 2023a, 2023b, this volume) and so should represent a sensitive, high-resolution tracer of dust-reprocessed UV light from young stars. Based on this, we develop criteria to select a larger sample of candidates. This selection is primarily based on the F330M − F335M color excess and yields a sample of 67 candidate embedded clusters in NGC 7496. By comparing the F300M − F335M colors of this sample to optically selected clusters in the PHANGS-HST catalog that have ages determined through SED fitting of five-band UV-optical photometry, we estimate that the embedded clusters are likely to be younger than ∼2 Myr.

We find that our new sample may significantly increase the census of young clusters from the PHANGS-HST catalog; the number of clusters younger than 2 Myr could be increased by a factor of 2. A more careful analysis of the selection functions and completeness of both the HST and JWST cluster samples will be required to provide an accurate assessment of the fraction of young clusters that are embedded and missing from optical catalogs. The eight clusters in common between the two catalogs have very young SED ages (six are ∼1 Myr). These results underscore the importance of our new PHANGS–JWST imaging for studying the earliest stages of star and cluster formation.
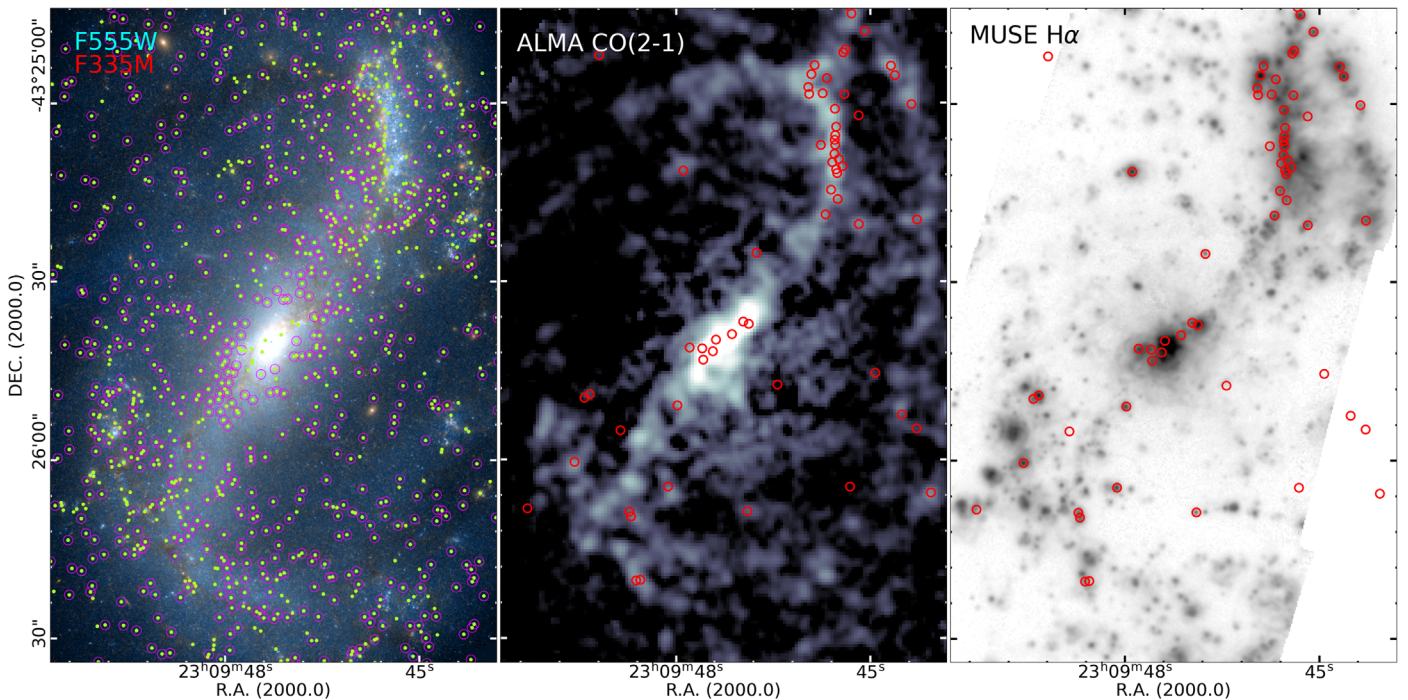
Figure 5. Left: combined HST F555W (blue) and JWST F335M (red) image. The green dots are sources detected in F335M that satisfy our color cut F300M − F335M > 0.3 (Section 3.3) but before performing any cut in magnitude. Sources shown in green without a magenta circle are the strongest PAH emitters and mostly found in the main dust lanes within the spiral arms. Sources with an additional magenta circle are those that have F300M − F335M between 0.3 and 0.7 and F335 > 24.5; i.e., they are both fainter and have larger color uncertainties (magenta box in Figure 2). This figure shows that when we select only the brightest sources with the largest color excesses, sources that tend to coincide with minor dust lanes in the galaxy, i.e., potentially fainter embedded clusters, are excluded. Middle: CO(2–1) ALMA map, with resolution of ∼1 with the 67 embedded cluster candidates (red circles). Right: MUSE Hα map with a resolution of ∼0″7 and the 67 candidates. Note that the sample is well correlated with Hα and CO(2–1) peaks.
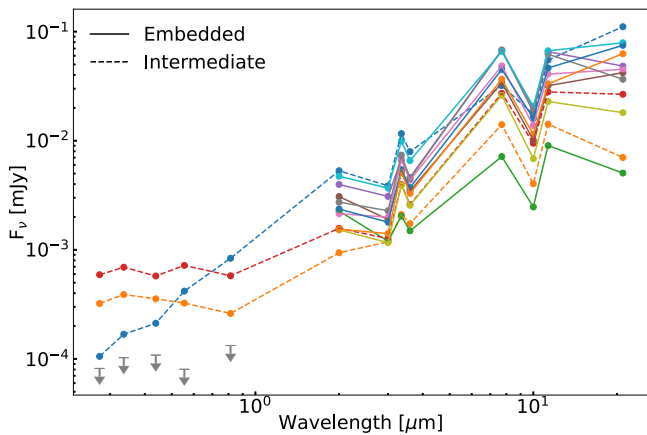
Figure 6. Preliminary UV-IR SED of the 12 embedded prototype clusters (Section 3.1). Prototypes classified as partially embedded or "intermediate" are shown with dashed lines, and embedded clusters are shown as solid lines. For objects that are not detected in the HST bands, we show upper limits with gray arrows. These preliminary SEDs are constructed with fluxes measured with the same aperture in all bands, which leads to an underestimate of the flux in the MIRI bands and without aperture correction. Nevertheless, two features in the SEDs of embedded clusters are clearly seen: PAH emission at 3.3 μm and silicate absorption at 10 μm.

Preliminary optical/infrared SEDs for the visually selected prototype candidates show PAH emission and possible silicate absorption. The CI measurements confirm that the majority of our 67 sources are more extended than stars/point sources. These characteristics provide additional evidence that most of our selected candidates are star clusters. We also take a first look at the 2 and 3 μm LFs for our sample and estimate stellar masses, finding values of 10^4–$10^5 M_\odot$.

The strongest and brightest PAH emitters are mainly located in prominent dust lanes within the main spiral arms of the galaxy, next to young optically detected clusters from PHANGS-HST. The spatial distribution of our candidates shows that they are also correlated with Hα and CO(2–1) emission.

In future work, we will expand this analysis to all 19 galaxies in the PHANGS–JWST sample and examine the completeness of samples based on the F300M – F335M color excess for selecting young embedded star clusters. Significant effort will be required to develop techniques to obtain robust total fluxes across the 13 PHANGS-HST and JWST filters from 2750 Å to 2 μm due to the factor of 10 decrease in resolution. Such techniques are needed to produce SEDs appropriate for constraining the physical properties of these clusters through the fitting of stellar population and dust models. Ultimately, a complete census of star clusters from PHANGS-HST and JWST will enable basic unsolved problems in star formation and cluster evolution to be addressed through new constraints on the initial cluster mass function, star cluster formation efficiencies, and feedback timescales associated with the clearing of the natal gas and dust.

ORCID iDs

M. Jimena Rodríguez https://orcid.org/0000-0002-0579-6613
Janice C. Lee https://orcid.org/0000-0002-2278-9407
B. C. Whitmore https://orcid.org/0000-0002-3784-7032
David A. Thilker https://orcid.org/0000-0002-8528-7340
Daniel Maschmann https://orcid.org/0000-0001-6038-9511
Rupali Chandar https://orcid.org/0000-0003-0085-4623
Sinan Deger https://orcid.org/0000-0003-1943-723X
Médéric Boquien https://orcid.org/0000-0003-0946-6176
Daniel A. Dale https://orcid.org/0000-0002-5782-9093
Kirsten L. Larson https://orcid.org/0000-0003-3917-6460
Thomas G. Williams https://orcid.org/0000-0002-0012-2142
Hwihyun Kim https://orcid.org/0000-0003-4770-688X
Eva Schinnerer https://orcid.org/0000-0002-3933-7677
Erik Rosolowsky https://orcid.org/0000-0002-5204-2259
Adam K. Leroy https://orcid.org/0000-0002-2545-1700
Eric Emsellem https://orcid.org/0000-0002-6155-7166
Karin M. Sandstrom https://orcid.org/0000-0002-4378-8534
J. M. Diederik Kruijssen https://orcid.org/0000-0002-8804-0212
Kathryn Grasha https://orcid.org/0000-0002-3247-5321
Elizabeth J. Watkins https://orcid.org/0000-0002-7365-5791
Ashley. T. Barnes https://orcid.org/0000-0003-0410-4504
Mattia C. Sormani https://orcid.org/0000-0001-6113-6241
Jaeyeon Kim https://orcid.org/0000-0002-0432-6847
Gagandeep S. Anand https://orcid.org/0000-0002-5259-2314
Mélanie Chevance https://orcid.org/0000-0002-5635-5180
F. Bigiel https://orcid.org/0000-0003-0166-9745
Ralf S. Klessen https://orcid.org/0000-0002-0560-3172
Hamid Hassani https://orcid.org/0000-0002-8806-6308
Daizhong Liu https://orcid.org/0000-0001-9773-7479
Christopher M. Faesi https://orcid.org/0000-0001-5310-467X
Yixian Cao https://orcid.org/0000-0001-5301-1326
Francesco Belfiore https://orcid.org/0000-0002-2545-5752
Ismael Pessa https://orcid.org/0000-0002-0873-5744
Kathryn Kreckel https://orcid.org/0000-0001-6551-3091
Brent Groves https://orcid.org/0000-0002-9768-0246
Jérôme Pety https://orcid.org/0000-0003-3061-6546
Rémy Indebetouw https://orcid.org/0000-0002-4663-6827
Oleg V. Egorov https://orcid.org/0000-0002-4755-118X

Guillermo A. Blanc ⬤ https://orcid.org/0000-0003-4218-3944
Toshiki Saito ⬤ https://orcid.org/0000-0002-2501-9328
Annie Hughes ⬤ https://orcid.org/0000-0002-9181-1161

References

Anand, G. S., Lee, J. C., Van Dyk, S. D., et al. 2021, MNRAS, 501, 3621
Astropy Collaboration, Price-Whelan, A. M., Lim, P. L., et al. 2022, ApJ, 935, 167
Astropy Collaboration, Price-Whelan, A. M., Sipőcz, B. M., et al. 2018, AJ, 156, 123
Astropy Collaboration, Robitaille, T. P., Tollerud, E. J., et al. 2013, A&A, 558, A33
Bradley, L., Sipőcz, B., Robitaille, T., et al. 2022, astropy/photutils: v1.5.0, Zenodo, doi:10.5281/zenodo.6825092
Chandar, R., Whitmore, B. C., Kim, H., et al. 2010, ApJ, 719, 966
Chastenet, J., Sutter, J., Sandstrom, K. M., et al. 2023a, ApJL, 944, L12
Chastenet, J., Sutter, J., Sandstrom, K. M., et al. 2023b, ApJL, 944, L11
Corbelli, E., Braine, J., Bandiera, R., et al. 2017, A&A, 601, A146
Crapsi, A., van Dishoeck, E. F., Hogerheijde, M. R., Pontoppidan, K. M., & Dullemond, C. P. 2008, A&A, 486, 245
Dale, D. A., Boquien, M., Barnes, A. T., et al. 2023, ApJL, 944, L23
Deger, S., Lee, J. C., Whitmore, B. C., et al. 2022, MNRAS, 510, 32
Elmegreen, B. G. 2008, ApJ, 672, 1006
Emsellem, E., Schinnerer, E., Santoro, F., et al. 2022, A&A, 659, A191
Fall, S. M. 2006, ApJ, 652, 1129
Grasha, K., Calzetti, D., Bittle, L., et al. 2018, MNRAS, 481, 1016
Grasha, K., Calzetti, D., Adamo, A., et al. 2019, MNRAS, 483, 4707
Großschedl, J. E., Alves, J., Teixeira, P. S., et al. 2019, A&A, 622, A149
Johnson, K. E., Indebetouw, R., & Pisano, D. J. 2003, AJ, 126, 101
Kim, J., Chevance, M., Kruijssen, J. M. D., et al. 2021, MNRAS, 504, 487
Kim, J., Chevance, M., Kruijssen, J., et al. 2023, ApJL, 944, L20
Kourkchi, E., Courtois, H. M., Graziani, R., et al. 2020, AJ, 159, 67
Kruijssen, J. M. D. 2012, MNRAS, 426, 3008
Lada, C. J., & Lada, E. A. 2003, ARA&A, 41, 57
Larsen, S. S. 2009, A&A, 494, 539
Lee, J. C., Ly, C., Spitler, L., et al. 2012, PASP, 124, 782
Lee, J. C., Sandstrom, K. M., Leroy, A. K., et al. 2023, ApJL, 944, L17
Leroy, A. K., Bolatto, A. D., Ostriker, E. C., et al. 2018, ApJ, 869, 126
Leroy, A. K., Schinnerer, E., Hughes, A., et al. 2021, ApJS, 257, 43
Ly, C., Lee, J. C., Dale, D. A., et al. 2011, ApJ, 726, 109
Messa, M., Calzetti, D., Adamo, A., et al. 2021, ApJ, 909, 121
Sandstrom, Koch, E. W., Leroy, A. K., et al. 2023a, ApJL, 944, L8
Sandstrom, Chastenet, J., Sutter, J., et al. 2023b, ApJL, 944, L7
Shaya, E. J., Tully, R. B., Hoffman, Y., & Pomarède, D. 2017, ApJ, 850, 207
Thilker, D. A., Whitmore, B. C., Lee, J. C., et al. 2022, MNRAS, 509, 4094
Turner, J. A., Dale, D. A., Lee, J. C., et al. 2021, MNRAS, 502, 1366
Whitmore, B. C., Chandar, R., Bowers, A. S., et al. 2014a, AJ, 147, 78
Whitmore, B. C., Chandar, R., Rodríguez, M. J., et al. 2023, ApJL, 944, L14
Whitmore, B. C., Zhang, Q., Leitherer, C., et al. 1999, AJ, 118, 1551
Whitmore, B. C., Brogan, C., Chandar, R., et al. 2014b, ApJ, 795, 156
Whitmore, B. C., Lee, J. C., Chandar, R., et al. 2021, MNRAS, 506, 5294